Supplemental material

Nanocrystalline and stacking-disordered β-cristobalite $AlPO_4$ chemically stabilized at room temperature: synthesis, physical characterization, and X-ray powder diffraction data

B. Peplinski, B. Adamczyk, P. Formanek, C. Meyer, O. Krüger, H. Scharf, S. Reinsch, M. Ostermann, M. Nofz, C. Jäger, C. Adam, F. Emmerling

Content

S1. DETAILED DESCRPTION OF THE APPLIED SYNTHESIS PROCEDURE

a. The undoped non-stoichiometric aluminum phosphate precipitate

79.7 g (0.33 mol) $AlCl_3 \cdot 6H_2O$ and 34.5 g (0.3 mol) $NH_4H_2PO_4$ were dissolved in 300 mL and 100 mL distilled water, respectively. Both solutions were combined. 32% aqueous NH_3 was added dropwise under constant stirring till the solution became jelly-like and the pH of the solution was between 4.8 and 5.0. In the given synthesis 57 mL NH_3 were consumed. The gel was separated from the residual solution by centrifugation then dried on air for 2 days at room temperature and another 2 days at 70 °C. The resulting semi-finished (*SF*) product was named *SF*-70. An XRD analysis of *SF*-70 proved that the aluminum- and phosphor containing component is X-ray amorphous but intermixed with a large mass fraction of well-crystallized NH_4Cl. An XRF-analysis of *SF*-70 yielded a value of 1.156 and of 27.5 wt.%, for the Al/P-ratio and for the chlorine content, respectively. That means, that the NH_4Cl content was about 41 wt.%, i.e. 62 vol.%. The importance of this high volume fraction value will be clarified in section S9. According to data generated by the thermodynamic calculation program 'HSC Chemistry v. 6.12' by Roine A. (2007) the sublimation and disintegration of NH_4Cl starts at 240 °C and is completed at 340 °C. However, a preliminary attempt to reduce the ammonium chloride content of a small portion of *SF*-70 by prolonged heating at 360 °C h in a large muffle furnace with switched-off forced circulation did not lead to satisfactory results. However, the following procedure proved to be successful, as it led to a total mass loss of about 50 wt.%: Grinding the whole batch of the *SF*-70 powder in an agate ball mill, spreading

it in a thin layer on dishes and tempering in a muffle furnace at 380 °C for 5 hours with moderate forced venting. This thermally cleaned non-stoichiometric aluminum phosphate powder was named *SF*-380 and analyzed by XRF. Its chlorine content was found to be 0.65 wt.%, only. To reduce the chlorine content to an even lower value, *SF*-380 was subjected to the following washing procedure: (1) grinding the dried powder in an agate mill for 1 hour followed by (2) elutriating in 200 mL distilled water stirring constantly at 50 °C for 1 hour, (3) centrifuging, drying on air for 1 day at room temperature and for another day at 70 °C. This washing procedure should be repeated another two times. Therefore, the name of this substance was changed to *SF*-380-3w. An XRF analysis of SF-380-3w determined a value of 1.14 (mol/mol) for its Al/P-ratio and 0.1 wt.% for its chlorine content. An independent determination of the Al/P-ration by ICP-OES gave exactly the same result. An independent determination of the chlorine content of *SF*-380-3w was carried out by ion chromatography (IC) yielding a value of 0.07 wt.%.

b. Calcium nitrate tetra urea

$Ca(NO_3)_2 \bullet 4CO(NH_2)_2$ was crystallized by adding a stoichiometric amount of solid urea to a saturated aqueous $Ca(NO_3)_2 \bullet 4H_2O$ solution, stirring it and letting it dry at air at 40 °C until a crystalline powder was formed, that was subsequently dried at 85 °C for 6 hours, see Lehr *et al.* (1991). This batch of $Ca(NO_3)_2 \bullet 4CO(NH_2)_2$ powder was named Ca-NTU. Its crystallinity and the absence of any crystalline impurity phases were proven by XRD and light microscopy.

c. Doping

To study the influence of the ratio of the mass fractions $w_{Ca\text{-}NTU}/w_{AlPO4}$ and w_{Ca}/w_{AlPO4}, four types of blends (called *Z*, *Q*, *H* and *M* as explained in section II.A) were generated. All these weight fraction values refer to the oven-dry mass of the $AlPO_4$ component. This means, that each time before a certain amount of the $AlPO_4$-component *SF*-380-3w was doped with Ca-NTU, it was first weighed, then put in a Pt-dish and dried at 380 °C for one hour in a dry-box to get rid of the adsorbed atmospheric moisture, and then, immediately after being removed from the dry-box, weighed again. The observed weight loss ranged from 20 to 22 wt.% in all cases.

d. Grinding and homogenizing, dispersion of the calcium component

The doped aluminum phosphate powder was carefully pre-homogenized in a previously unused manual agate mortar with perfectly smooth surfaces. Subsequently, it was homogenized in a mixer mill, Retsch 'MM301', equipped with a closed grinding beaker and ball, both made from zirconia. The used frequency of vibration was 25 s^{-1}. The grinding time for a single grinding step was one minute. After each grinding step the powder was completely recovered from the beaker and after washing and drying the beaker the powder was refilled again. This procedure was repeated another three times, thus the total grinding time was four minutes. Not only the doped aluminum phosphate powders used for the synthesis of the *Q*-, *H*- and *M*-series were submitted to this procedure but also the undoped powder used for the synthesis of the *Z*-series.

e. Pelletizing

After doping and homogenizing, the doped aluminum phosphate powder was pelletized in a hydraulic press for the following three reasons: To (1) ensure that the same mass of doped aluminum phosphate is dealt with in each calcination treatment; (2) make the handling of the powder during charging and discharging the tube furnace safer and less time-consuming; (3) improve the heat transport inside the powder by making its packing denser, more homogeneous and reproducible. Each pellet had a mass of 290(5) mg, a diameter of 12 mm

and was less than 2 mm thick. A single batch of doped and homogenized powder yielded 6 pellets.

f. Calcination
Each single pellet was crystallized individually by fast heating up, holding it at the targeted temperature for a retention time of exactly 20 minutes and then quenching it to room-temperature. This (T,t)-program was realized by an experimental set-up (Peplinski *et al.*, 2013) that allows sample heating rates of up to 1000°/min and accurate temperature control of the pellet. During this heat treatment, a single pellet lies on a palladium foil (18 x 14 x 0.025 mm, 75 mg) that is supported by the unfixed ends of two horizontal and parallel twin-hole corundum tubes ($Ø_{outer}$= 1.6 mm, $Ø_{inner}$= 0.4 mm for each of the twin holes, L = 300 mm). The opposite ends of these corundum tubes are fixed to a steady support. The sample temperature is measured directly at the pellet and digitally processed during the whole (T,t)-program. The computer-controlled horizontal tube furnace is mounted on rails and can be moved along these rails by an electrical drive. While the tube-furnace is pre-heated to the targeted temperature it is still far away from the $AlPO_4$ pellet. Not until after the temperature of the furnace is equilibrated the electrical drive is switched on and moves the furnace along the rails from its remote position towards the $AlPO_4$ pellet until the center of its hot zone coincides with the position of the pellet. At the end of the retention time the electrical drive moves the tube furnace away from the pellet to its initial position. The calcined pellet was weighed, pulverized in a hand agate mortar and named as described in section II.A.

S2. EXPERIMENTAL – ELECTRON MICROSCOPIC METHODS AND EDX MAPPING

a. Equipment
TEM images were recorded with a Zeiss Libra200 TEM instrument operated at 200 kV. The SEM images were recorded with a Zeiss Neon40 SEM instrument operated at 3 kV. A secondary electrons detector or an in-lens detector were used, whichever provided images of higher quality. The EDX maps were recorded with a Zeiss Ultra SEM instrument operated at 6 kV and equipped with a Bruker XFlash5060 EDX spectrometer.

b. Sample preparation
About 1 mg of powder was dispersed in 200 microliter of ethanol and ultrasonicated for 2 min. For TEM specimens 2 microliters of suspension were placed on a 200 mesh TEM grid with 20 nm carbon film and dried in air at ambient temperature. For SEM and EDX specimens 1 microliter of suspension was placed on 5 mm x 5 mm silicon wafer, dried in air at ambient temperature and coated with ca. 20 nm amorphous carbon film using a Leica SCD500 coater to reduce charging in the electron beam.

c. Data collection and evaluation
Our *preliminary* TEM investigations of sample *H*-871 had shown that the title compound is prone to beam damage. An electron dose rate of 32,000 e/nm^2/s leads to amorphisation of the *β*-cristobalite $AlPO_4$ nanocrystals within a few seconds. The amorphisation starts at the surface of the nanoparticles and progresses through the entire particle. After approx. 10 seconds (dose 320,000 e/nm^2) the crystalline order in the nanoparticles is completely destroyed: Previously well discernible lattice fringes and reflections in the diffraction pattern disappear completely, while the shape of the particles remains unaffected. Consequently, in all following investigations lower beam intensity was used, which caused increased noise in images at high magnification. As an example, Figures S2 to S4 are quite noisy due to using a

comparably low electron dose of 32,000 e/nm^2 and stopping the data collection just before the onset of the radiation damage.
Despite of proper coating the specimens with an amorphous carbon film, some larger agglomerates were charged under the electron beam. This led to stripes in some SEM images (see Figure S5). However, this does not prevent correct judgment on the shape of the particles.
The carbon peak (from coating) observed in the EDX spectra overlaps with the Ca-*L* peak. Therefore, only the Ca-*K* peak was used for the element maps (see section S.11). The silicon peak observed in some EDX spectra originates from the silicon wafer used as a substrate in the SEM investigations. The EDX maps were processed with ESPRIT 1.9 software by Bruker.

S3. EXPERIMENTAL – NUCLEAR MAGNETIC RESONANCE SPECTROSCOPY (NMR)

^{31}P solid-state NMR experiments were performed on a Bruker Avance 600 spectrometer (B_0 = 14.1 T). All experiments were carried out at room temperature using a 4 mm magic angle sample spinning (MAS) probe. The MAS frequency was 12.5 kHz. Data analysis was performed with the software TopSpin 2.1.
^{31}P MAS NMR spectra were recorded at a Larmor frequency of 242.9 MHz using a 90° pulse length of 4.5 µs. The repetition time was 300 s, and 8 to 16 scans were accumulated. ^{31}P chemical shifts (δ) are reported relative to hydroxyapatite as secondary standard at 2.3 ppm.
^{27}Al MAS NMR measurements were run at a Larmor frequency of 156.3 MHz using a selective 90° pulse of 2 µs and a repetition time of 90 s. 4 to 8 scans were accumulated. ^{27}Al chemical shifts (δ) are reported relative to the narrow octahedrally co-ordinated signal of YAG at 0.6 ppm.
In addition, ^{31}P{^{27}Al} TRAPDOR (TRAnsfer of Population in DOuble Resonance) experiments were performed on synthesis product *H*-1292 to prove which of the ^{31}P NMR signals around 0 ppm (typical calcium orthophosphate range) correspond to P-O-Al bonding motives that are characteristic for the $Ca_9Al(PO_4)_7$ phase segregating at high calcination temperatures. The ^{31}P 90° and 180 ° pulse lengths were shortened to 2.3 and 4.6 µs and the ^{27}Al TRAPDOR pulses were applied before and after the ^{31}P echo pulse. The total echo time prior the data acquisition was set to 52 rotor periods or 4.16 ms. The repetition time was 180 s and 64 scans were accumulated.

S4. EXPERIMENTAL – THERMOANALYTICAL METHOS (TG AND DTA)

Thermal gravimetric analyses (TG) and differential thermal analyses (DTA) were simultaneously recorded by a thermo-balance SETARAM TAG 24 (Setaram, Caluire, France) with an 1600 °C equipment. Measurements were conducted in flowing synthetic air (45 mL min^{-1}) on powdered samples (initial weight ≈ 20 mg) placed in open corundum crucibles (100 µL) at a heating rate of 10 K/min. Cooling to room temperature was carried out at -10 K/min followed by one repetition of this heating and cooling procedure. The sample mass was recorded with an accuracy of ±0.01 mg.

S5. EXPERIMENTAL – X-RAY FLUORESCENCE SPECTROSCOPY (XRF)

XRF analyses were carried out with a MagiXPro instrument (Panalytical) equipped with a rhodium sealed tube operated at 60 kV and 60 mA and with Bragg crystal analyzer. Before

being analyzed by XRF, the powder samples were compressed into the shape of dense solid discs having a diameter of 32 mm and a height of 4 mm.

S6. EXPERIMENTAL – OPTICAL EMISSION SPECTROSCOPY ICP-OES

Inductively coupled plasma optical emission spectroscopy (ICP-OES) measurements were performed from undiluted solutions according to the respective standard, ISO (2007), with a Thermo Scientific iCAP 7400 instrument. Measurement wavelengths are stated in nm and were as follows: Al (185.593; axial), P (213.618; axial), Na (589.592, radial), K (766.490, radial), Ca (396.847, radial).The samples were dissolved with microwave-assisted digestion according to the respective standard, ISO (1995). For this, the samples were weighed in with an accuracy of ±0.1%, mixed with 1.2 mL of concentrated nitric acid (HNO_3), 3.6 mL concentrated hydrochloric acid (HCl), and 0.5 mL double-distilled water.

S7. EXPERIMENTAL – ION CHROMATOGRAPHY (IC)

Ion chromatographic measurements were carried out using the instrument 883 Basic IC PLUS (Metrohm).

S8. EXPERIMENTAL – GAS SORPTION METHODS

Gas sorption analyses were carried out with an Accelerated Surface Area and Porosimetry System (ASAP) ASAP2010 S.No. #371 made by Micromeritics, Norcross, USA. Prior to the gas sorption analysis the sample was in situ heated at 180 °C for 1 h with vacuum applied. For the adsorption measurements nitrogen gas was used.

S9. MORPHOLOGY AND POROSITY OF THE PARTICLES

The morphology of particles of the title compound was investigated by SEM and TEM. Figure S5(a) to (d) display representative images of three synthesis products. They resemble those of the semi-finished product *SF*-380-3w shown in Figure S6(a) to (c). These images proof the presence of mesopores in *both* substances. This finding has been confirmed by the results of gas sorption analyses (see Table SIII and Figure S7). The mass loss of 21% observed upon heating the semi-finished product *SF*-380-3w has been quantitatively confirmed by dozens of thermogravimetric and gravimetric measurements (see section S1.*c.* Doping) and can be undoubtedly attributed to the reversible release of adsorbed and condensed atmospheric humidity. The presence of mesopores with a most frequent diameter around 17 nm (see Table SIII and Figure S7) allows the conclusion that capillary condensation essentially contributes to this moisture adsorption. The total volume fraction of the micro- and mesopores in *SF*-70 and *SF*-360-3w was estimated by three methods: (1) By the volume fraction of the NH_4Cl content in the semi-finished product *SF*-70 (see section S1.*a*); (2) From the mass loss caused by the release of moisture upon (vacuum) drying of the semi-finished *SF*-380-3w (see Table SIII, line A); And (3) from the total pore volume determined for the semi-finished *SF*-380-3w by gas adsorption (see Table SIII, line B). The first, second and third method yield values of 62, 49.5 and 48 vol.%, respectively. The difference between the first and the last two values most likely reflects the partial loss of pore volume caused by submitting *SF*-70 to prolonged heating at 360°C and subsequently to a

triple washing procedure as well as four grinding procedures, before it became *SF*-380 and finally *SF*-380-3w (see section S1.*a*). These three large values of the (open) pore volume support the visual impression gained from the electron microscopic images (see Figures S5 and S6) that the particles of the semi-finished product *SF*-380-3w have a morphology resembling a natural sponge, i.e. an elastic body full of open pores and channels allowing water to penetrate and circulate. The high degree of elasticity associated with this specific microstructure makes the particles of the semi-finished product *SF*-380-3w highly resistant against the massive mechanical impact associated with the grinding and homogenization of the doped aluminum phosphate powder (see section S1.*d*). This elasticity explains why the morphology of the synthesis products, i.e. of the title compound (see Figure S5), still resembles the morphology of the semi-finished product *SF*-380-3w (see Figure S6). The fact that the semi-finished product *SF*-380-3w is sponge-like, with ca. 50% of its volume permanently filled with water, together with the fact, that the calcium nitrate tetra urea crystals are highly water-soluble (Lehr *et al.*, 1991) sheds also new light on the mechanism by which the tiny amount of Ca-rich dopant is dispersed across the aluminum phosphate. What might have appeared to be a solid state reaction between two powders turns out to include an intermediate step resembling an impregnation of the sponge-like particles of the semi-finished product *SF*-380-3w with an aqueous solution of calcium nitrate tetra urea. In this context, the milling is essential for the dissolution as well as for the intra-particle and inter-particle equilibration of the concentration of the aqueous solution. The strong dependence of the crystallization temperature on the calcium content mentioned in section III.B implies that the better the calcium component is dispersed across (the surface of) all aluminum phosphate particles the better the crystallization of the title compound will be synchronized across the entire aluminum phosphate pellet during calcination.
And in the light of what is said at the very beginning of section III.C this means: The better defined will be the structural parameters of the quenched synthesis products.

S10. DISTINCTIVE 'REAL STRUCTURE' FEATURES AND THEIR CONSEQUENCES

The diffraction patterns of the title compound visualized in Figures 1, 2, 4, 8(b) and 11(a) contain only diffraction lines with low peak height but a very intensive background which is several times higher than the background level observed in the diffraction patterns of the reference sample (see Figure 8(a)) and of the synthesis product *H*-1292 (see Figure 3) as well as in the scattering curve of the empty zero-background sample holder (see Figure 1). In this context it is worth remembering, that a high background in a diffraction pattern is not necessarily a proof of a high amorphous content. 'Several factors contribute to scattering and diffraction at angles other than those of the discrete Bragg reflections… . The more important effects include (1) lattice imperfections of various kinds, … this … includes all departures of the actual scattering centers in a structure from the points of the ideal lattice. … *Randomness of stacking of the layers in a layer structure* or imperfections in the mutual orientations of the layers *lead both* to broadening of certain reflections and *to increased background scatter, ...*' Klug and Alexander (1974-b). Or as Honkimäki and Suorti (1999-a) put it 'The background arises from disorder ... . The structure of the crystal is distorted by *positional* or substitutional *disorder* and by thermal motion of the atoms. These disrupt the perfect order of the crystal lattice, *decreasing the intensity of Bragg reflections and redistributing the scattering to diffuse background*.'
It were the *β*-cristobalite forms of well-crystallized SiO_2 and $AlPO_4$ powder samples where a so far unknown kind of disorder was observed for the first time by Wright and Leadbetter (1975). Its nature was recently unraveled by Yuan and Huang (2012), who described it as a

permanent flipping of the SiO_2 or $AlPO_4$ rings between two different ring conformations at a rate of several tens of femtoseconds. This very special kind of disorder manifests itself through the occurrence of intensive diffuse scattering in selected area electron diffraction (SAED) patters which are collected during in situ high-temperature transmission electron microscopy investigation. For this study well-crystallized and stacking disorder-free *single crystals* of *α*-cristobalite SiO_2 and $AlPO_4$ were used and the specimen temperatures were kept well above the reversible *α-β* phase transition (Hua et al., 1988; Phillips *et al.,* 1993).

In high temperature X-ray powder diffraction patterns of the *β*-cristobalite form of well-crystallized and stacking disorder-free *α*-cristobalite SiO_2 or $AlPO_4$ samples which were collected at temperatures well above the *α-β* phase transition this specific kind of positional dynamical disorder manifests itself as well. However, to describe these diffraction data, unusual large Debye-Waller temperature factors which include a very large *temperature independent* term have to be used (Wright and Leadbetter, 1975). Thus for *β*-cristobalite SiO_2 at 300°C, a Debye-Waller temperature factor B_{Si} = 3.56 Å^2 results that is more than seven times larger than the B_{Si} value for quartz at the same temperature. Extrapolation to 200°C or to room temperature yield still large values of 3.24 or 2.95 Å^2. As Wright and Leadbetter state in the abstract of their paper that 'the *β*-cristobalite phase of $AlPO_4$ is similarly disordered … .' it is reasonable to assume that this very specific kind of positional dynamical disorder equally occurs in the title compound of the present paper, too. As any attempt to determine the degree of crystallinity and the amorphous fraction in the synthesis products by XRD would most likely be based on the integral intensity of the 220 reflection of the title compound it is worth mentioning, that Debye-Waller temperature factors B_{Al} and B_P as large as 3.24 or 2.95 Å^2 have the capacity to change the results of these analyses by 22 or 20%, respectively.

In addition to those kinds of disorder mentioned so far, in the case of the title compound two more kinds of disorder have to be taken into account. The first is the positional static disorder which is associated with the very high degree of *random* stacking disorder, see Figures 8(b) and 8(c), as well as similar powder diffraction pattern simulations carried out by Weiss and Chapkova (1999) for ZnS and CdS. The second is the substitutional static disorder associated with a partial replacement of phosphorus ions by aluminum ions and the resulting distortion of the coordination tetrahedral that are likely to occur, see Stosser et al. (1989). According to the quotation from Honkimäki and Suorti (1999-a) given above, these two effects will further enhance the redistribution of intensity from the Bragg reflections to the background.

And finally, an underdetermination of the experimentally determined intensity values of the broadened Bragg reflections is likely to occur due to thermal diffuse scattering (TDS) effects which are described by the Debye-Faxen-Waller theory, see Klug and Alexander (1974-a), Warren (1969) as well as Honkimäki and Suortti (1999-b).

To summarize, there is presently no sound basis for extracting information on the degree of crystallinity of the synthesis products from the intensity data visualized in Figure 7. However, the intensity data determined on samples from the *M*-series are practically identical with that of the H-series, except for a shift of the whole curve by 40 K towards lower calcination temperatures. This means that doubling the Ca content does not further increase the degree of crystallinity of the synthesis products and might be an indication that the degree of crystallinity has reached its maximum value already in the synthesis products of the *H*-series. This interpretation is supported by the whole of the electron microscopic results, as the images shown in Figures S2 to S6 as well as images gained from a considerable number of additional samples give no indication of a large noncrystalline fraction.

S11. LOSS OF HOMOGENEITY AT ELEVATED TEMPERATURE, SEGREGATION OF MINOR COMPONENT(S)

While SEM-EDXS maps of the title compound (synthesis product *H*-871) show no signs of an inhomogeneous distribution of any of the chemical components (see Figure S8), the SEM-EDXS maps of synthesis product *H*-1167 provide clear evidence for a segregation of a calcium-rich component (see Figure S9). As an example, the intensity of the Ca spectral line measured at the positions marked 1 and 2 in the SEM image of synthesis product *H*-1167 are 0 and 30 cps/eV, respectively, see the zoomed EDX spectra in Figure S9 (The scale of spectrum 2 is adjusted so that the area below the phosphorus peak in spectrum 1 and spectrum 2 are the same. If any calcium line is present at all in spectrum 1, it is not distinguishable from the background level of 2 cps/eV).
Figure 3 shows a high quality XRD pattern of synthesis product *H*-1292 that was collected by running the same specimen four times with a total counting time of 160 s per measuring point. It provides clear evidence for the presence of two minor crystalline components: $Ca_9Al(PO_4)_7$ and corundum. In the XRD-pattern of synthesis product *H*-1167, diffraction lines characteristic for $Ca_9Al(PO_4)_7$ were detected, too, although with a lower intensity. No corundum lines were observed. In the XRD-pattern of synthesis product *H*-1073 the intensity of the diffraction lines characteristic for $Ca_9Al(PO_4)_7$ is further reduced and very close to the detection limit. Finally, in the diffraction pattern of synthesis product *H*-1049 diffraction lines of $Ca_9Al(PO_4)_7$ could not be detected anymore.
In the ^{31}P-NMR spectrum of synthesis product *H*-1292 visualized in Figure 12(c) the group of several minor lines with chemical shifts ranging from +1.3 to -3.6 proves the presence of a compound of the type $Ca_9M^{3+}(PO_4)_7$, in the given case of $Ca_9Al(PO_4)_7$ (Mellier *et al.*, 2011). This interpretation has been further confirmed by ^{31}P{^{27}Al} TRAPDOR experiments that were performed on the synthesis product *H*-1292. They proved that the ^{31}P NMR signals around 0 ppm, a range typical for calcium orthophosphates, correspond to P-O-Al bonding. In addition, the presence of a minor corundum component was confirmed by ^{27}Al-NMR.
Note, that $Ca_9Al(PO_4)_7$ belongs to the large β-TCP/whitlockite/apatite-group within the even larger group of calcium orthophosphates. Differentiation between the numerous compounds of these groups is often difficult, as their chemical composition and crystallographic structure differ only slightly. However, compounds of the $Ca_9M^{3+}(PO_4)_7$ –type (M^{3+}=Al^{3+},Fe^{3+},Ga^{3+},…) show crystallographic specifics (Yoshida *et al.*, 2006; Mellier *et al.*, 2011) and, therefore, even a small mass fraction of crystalline $Ca_9Al(PO_4)_7$ segregated in an aluminum phosphate matrix can be *unambiguously identified* both by XRD and ^{31}P-NMR.
The main component of synthesis product *H*-1292 is α-cristobalite $AlPO_4$ and the presence of the two minor components, $Ca_9Al(PO_4)_7$ and corundum, in this synthesis product documents itself in the fact, that the integral intensity of the 220 reflection of this main component is 14% smaller than the corresponding value for the reference sample (RS), see Figure 7. This value agrees well with the Al/P-ratio of the nonstoichiometric precipitate (Al/P=1.14, see section S1.a) and a Ca content of just 0.82 wt% used for the synthesis of *H*-1292.

S12. FIVE INFERENCES FROM THE PHYSICAL CHARACTERIZATION WHICH ARE CRUCIAL FOR THE REPRODUCIBILITY OF THE SYNTHESIS

- The temperature of the primary crystallization and thus the formation of the title compound strongly depend on the *locally* available amount of reactive calcium oxide. Therefore it is essential to disperse the dopant as *homogeneously* as possible at the micron and nanometer scale across the aluminum phosphate matrix.
- As a dopant, calcium nitrate tetra urea has a great advantage over calcium nitrate hydrate as it can be much better dispersed in the course of the applied grinding and homogenizing treatment.

- An open mesopore system in the aluminum phosphate component allows for extensive capillary condensation of atmospheric moisture. Thus it has an essential influence on the dispersal of any water-soluble calcium nitrate compound (dopant) and its fixation on the aluminum phosphate matrix. In the given synthesis procedure an open mesopore system was realized by the coprecipitation of amorphous aluminum phosphate and NH_4Cl followed by the thermal volatilization of the needle-like, dendritic or skeletal NH_4Cl crystals.
- The formation of calcium chloride should be avoided or at least minimized. To ensure this, the residual chlorine content of the aluminum phosphate matrix should be monitored and, if necessary, reduced by further process steps *before* the dopant is added.
- For a reproducible synthesis of the title compound in a well-defined structural and thermodynamical state it is essential that *all parts* of the doped aluminum phosphate powder are submitted to exactly the same (T,t) program during the calcination procedure.

S13. REFERENCES

Honkimäki V., and Suortti P. (**1999**). "Effects of instrument function, crystallite size, and strain on reflection profiles,", a: p. 46, b: pp. 50-52 in *Defect and Microstructure Analysis by Diffraction* edited by Snyder R.L., Fiala J. and Bunge H.J. (International Union of Crystallography Monographs on Crystallography, Vol. 10, Oxford University Press, N.Y.), pp. 41-58.

Hua G.L., Welberry T.R., Withers R.L., and Thomson J.G. (**1988**). „An electron diffraction and lattice-dynamical study of diffuse scattering in β-cristobalite, SiO_2," J. Appl. Crystallogr. **21**, 458-465.

ISO (**1995**). "Soil quality - Extraction of trace elements soluble in aqua regia," ISO 11466:1995, International Standard Organization.

ISO (**2007**). "Water quality - Determination of selected elements by inductively coupled plasma optical emission spectroscopy (ICP-OES)," ISO 11885:2007, International Standard Organization.

Klug H.P. and Alexander L.E. (**1974**). *X-ray Diffraction Procedures for Polycrystalline and Amorphous Materials* (Wiley, New York), 2nd ed., a: pp. 146-147, b: p. 489-490.

Lehr, J.R., Brown, E.H., Frazier, A.W., Smith, J.P., and Thrasher R.D. (**1991**). *Crystallographic properties of fertilizer compounds* (Tenessee Valley Authorities, National Fertilizer Development Center, Muscle Shoals, Alabama, USA).

Mellier, Ch., Fayon, F., Schnitzler, V., Deniard, P., Allix, M., Quillard, S., Massiot, D., Bouler, J.-M., Buyolim B., and Javier, P. (**2011**). "Characterization and properties of novel gallium-doped calcium phosphate ceramics," Inorg. Chem. **50**, 8252-8260.

Peplinski B., Adam C., Adamczyk B., Müller R., Schadrack R., Michaelis M., Emmerling F., Reuther H., Menzel M. (**2013**). "Evidence of formation of the tridymite form of $AlPO_4$ in some municipal sewage sludge ashes," Powder Diffraction Journal, **28**, Issue S2, S425-S435.

Roine, A. (**2007**), HSC Chemistry v. 6.12, www.hsc-chemistry.com and www.autotec.com.

Stosser, R., Nofz, M., and Ladwig, G. **(1989).** "Fe^{3+}- and Al-O^--Al species in $AlPO_4$ with cristobalite structure and tridymite structure," Zeitschrift für Chemie, **29,** 75-76.

Warren B.E. (**1969**). *X-ray Diffraction* (Addison-Wesley, Reading, Mass.), p. 193 ff.

Weiss Z., and Chapkova P. (**1999**). "Effect of stacking disorder on the profile of the powder diffraction line,", Figures 16.2(d) and 16.3(d) in *Defect and Microstructure Analysis by Diffraction* edited by Snyder R.L., Fiala J. and Bunge H.J. (International Union of Crystallography Monographs on Crystallography, Vol. 10, Oxford University Press, N.Y.), pp. 318-329.

Yoshida, K., Hyuga, H., Kondo, N., Kita, H., Sasaki, M., Mitamura, M., Hashimoto, and K., Toda, Y. (**2006**). "Substitution model of monovalent (Li, Na, and K), divalent (Mg), and trivalent (Al) metal ions for *β*-tricalcium phosphate," J.Am.Ceram.Soc. **89**, 688-690.

TABLES

TABLE SI. Results of the thermoanalytical investigation of selected synthesis products from *H*-860 to *H*-1292 and the reference sample (RS) carried out in the present project, as well as data for well-crystallized cristobalite-$AlPO_4$ published by Graetsch (2003), I = integral intensity of DTA signal (μV•s/mg), On. = Onset (°C), Max. = Maximum (°C), Off. = Offset (°C), m = DTA signal of *α-β* phase transition is completely *missing*.

sample	DTA run	DTA upon heating				DTA upon cooling			
		I	On.	Max.	Off.	I	On.	Max.	Off.
H-860	1.	m	m	m	m	m	m	m	m
||	2.	m	m	m	m	m	m	m	m
H-875	1.	m	m	m	m	m	m	m	m
||	2.	m	m	m	m	m	m	m	m
H-876	1.	m	m	m	m	m	m	m	m
||	2.	m	m	m	m	m	m	m	m
H-924	1.	m	m	m	m	m	m	m	m
||	2.	m	m	m	m	m	m	m	m
H-963	1.	m	m	m	m	m	m	m	m
||	2.	m	m	m	m	m	m	m	m
H-1024	1.	m	m	m	m	m	m	m	m
||	2.	m	m	m	m	m	m	m	m
H-1049	1.	0.6	136	146	160	-0.6	143	135	127
||	2.	0.6	135	145	162	-0.6	145	135	128
H-1167	1.	4.0	162	168	180	-4.4	158	152	142
||	2.	3.8	161	167	179	-4.8	158	152	141
H-1292	1.	9.6	199	207	220	-9.8	189	182	172
||	2.	9.5	198	206	219	-9.5	188	182	171
RS	1.	9.6	209	215	225	-10.7	190	185	170
||	2.	10.7	209	215	225	-10.6	191	185	170
Graetsch (2003)	1	-	202	-	-	-	187	-	-

TABLE SII. Summary of results provided by DTA, XRD, and ^{31}P-NMR analyses of eight synthesis products from the *H*-series and the reference sample (RS) in comparison with published reference values.
Note: 'm' stands for '*missing* of DTA signal of *α-β* phase transition, completely'. '*α*-c' and '*β*-c' stand for '*α*-cristobalite $AlPO_4$' and '*β*-cristobalite $AlPO_4$', respectively. Phill. (1993) stands for Phillips et al. (1993); δ^{31}P stands for the chemical shift of the cristobalite $AlPO_4$ line(s); 'split (A+B)' stands for 'the ^{31}P-NMR signal assigned to cristobalite $AlPO_4$ is *visibly* split into two components, A and B';
for further details see Figure 9 and Table SI, Figure 5(a), as well as Figures 10, 12 and S1.

sample	DTA		XRD	^{31}P-NMR				
	I	Onset (°C)	$2\theta_{220}$ (°)	split (A+B)	δ^{31}P (ppm)			$I_{integral}$
					@ I_{max}	line A	line B	$I_A : I_B$
H-860	m	m	35.341	no	-30.8	-	-	-
H-876	m	m	35.378	no	-30.8	-	-	-
H-924	m	m	35.440	no	-30.6	-	-	-
H-963	m	m	35.493	no	-30.4	-	-	-
H-1024	m	m	35.602	yes	-28.7	-28.3	-30.3	26 : 74
H-1049	0.6	136	35.677	yes	-28.1	-28.0	-30.0	38 : 62
H-1167	4.0	162	35.768	yes	-27.5	-27.5	-29.2	48 : 52
H-1292	9.6	199	35.798	yes	-26.9	-27.0	-28.4	85 : 15
RS	9.6	209	35.806	no	-26.8	-26.8	-	100 : 0
DTA reference value, Graetsch (2003)	-	202	-	-	-	-	-	-
XRD reference value for *β*-c @ 200°C, Graetsch (2003)	-	-	35.253	-	-	-	-	-
XRD reference value for *α*-c @ 200°C, Graetsch (2003)	-	-	35.675	-	-	-	-	-
XRD reference value for *α*-c @ RT, Graetsch (2003)	-	-	35.807	-	-	-	-	-
NMR reference value for *β*-c @ 225°C, Phill. (1993)	-	-	-	no	-30.7	-	-	-
NMR reference value for *α*-c @ RT, Phill. (1993)	-	-	-	no	-26.3	-	-	-

TABLE SIII. Porosity-related parameters of the semi-finished product *SF*-380-3w and of the title compound (synthesis product *H*-876) as determined by gas sorption methods:
A - mass loss (%) upon vacuum drying for 1h @ 180°C,
B - total pore volume (cm^3/g) determined by adsorption,
C - specific surface area (BET) (m^2/g),
D – DBJH, ads., i.e. most frequent pore diameter (nm) by adsorption

	SF-380-3w	*H*-876
A	21	5
B	0.426	0.135
C	79.1	25.5
D	16.6	12.8

FIGURE CAPTIONS

Figure S1. (Color online) ^{31}P-NMR spectra of the reference sample (RS) and eight synthesis products of the H-series, illustrating the sluggish conversion of the title compound into the thermodynamically stable α-cristobalite form of $AlPO_4$; The letters '*A*' and '*B*' mark two individual resonance lines assigned to cristobalite $AlPO_4$', See also Table SII and the fifth paragraph of section III.C.

Figure S2. (Color online) (a): HRTEM image of a sample of the title compound (synthesis product *H*-871), the three yellow-framed and numbered squares mark the three areas that are enlarged in Figures S3(1) to S3(3); (b): False color representation of the image shown in Figure S2(a), (c): Same as Figure S2(a) after applying a high-pass filter.

Figure S3. (Color online) (1) and (2): Enlarged details proving the presence of two different types of lattice fringes in the two areas marked by the yellow-framed squares nr. 1 and 2 in Figure S 2(a); (3): An enlarged detail proving the absence of lattice fringes in the area marked by the yellow-framed square nr. 3 in Figure S2(a). (To reduce the noise, the images were filtered with a 3x3 median filter, see section S2.*c*).

Figure S4. (Color online) (1) to (3): Results of a Fast Fourier Transformation (FFT) of the images depicted in Figure S3(1) to S3(3).

Figure S5. (Color online) Morphology of the title compound - synthesis products from three *different batches* visualized in SEM (a), (c) and (d) and in TEM (b); (a) and (b): *H*-871, (c): *H*-875, (d): *H*-887.

Figure S6. (Color online) Morphology and size of open mesopores of the semi-finished product *SF*-380-3w visualized by SEM; (a), (b) and (c) stand for three different subsamples taken from the same product.

Figure S7. (Color online) Differential pore volume distribution of the semi-finished synthesis product *SF*-380-3w (upper blue curve with circles) and of the title compound (synthesis product *H*-876, lower red curve with squares), determined by gas adsorption measurements, V – pore volume, d_p – pore diameter.

Figure S8. (Color online) SEM image, SEM-EDXS maps and EDX spectrum of the title compound - synthesis product *H*-871 (the EDX spectrum was collected from the red framed square area highlighted in the SEM image).

Figure S9. (Color online) SEM image, SEM-EDXS maps and EDX spectra from two different spot-areas of synthesis product *H*-1167 (the green EDX spectrum was collected from the green spot, marked '1', as highlighted in the SEM image and the red EDX spectrum was

collected from the red spot, marked ‘2’. The two spectra are scaled in such a way that the areas under the phosphorus peak are the same).

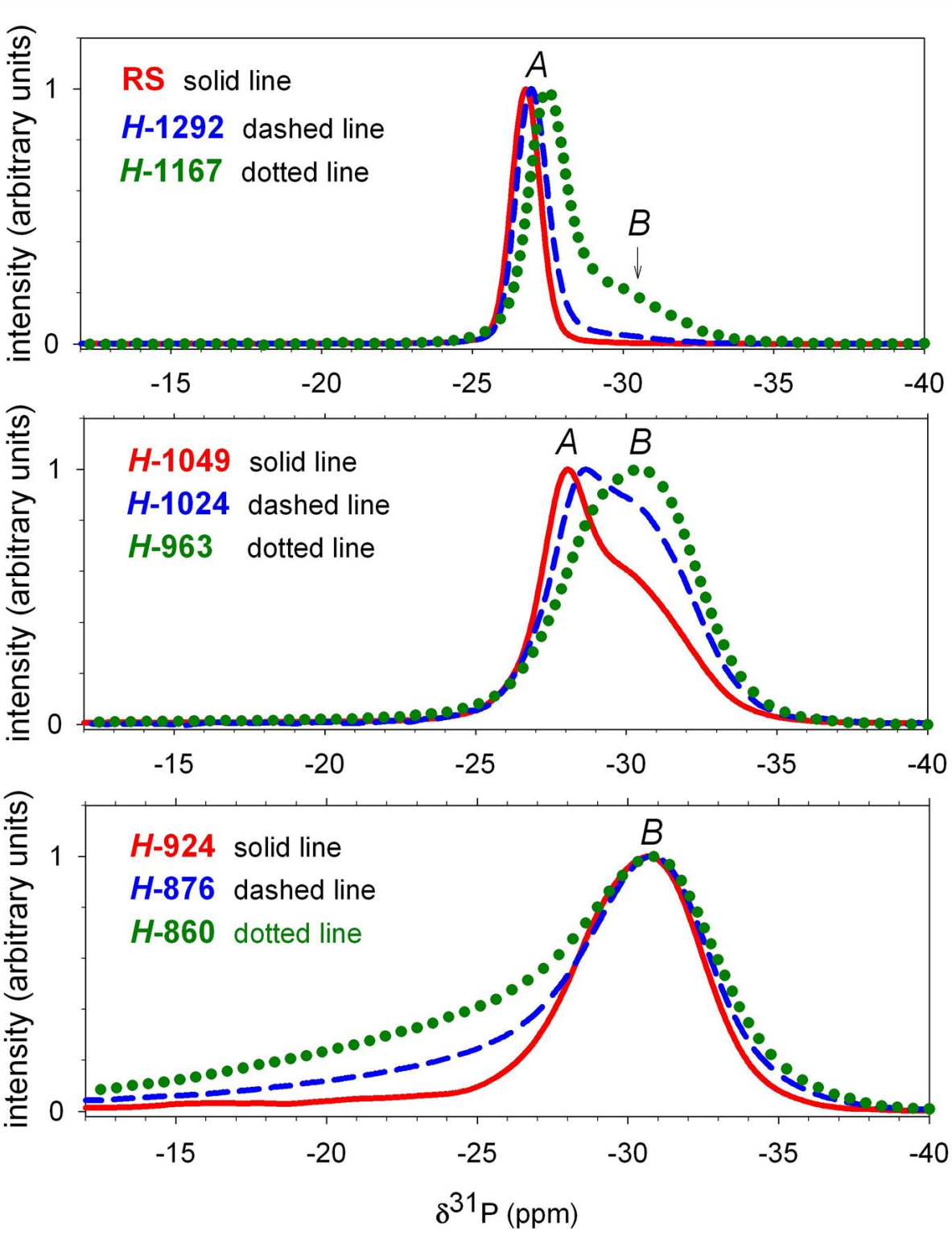

EPDIC15_Proc._Peplinski_Figure S1_(2017-05-16, 1.0 MB).tif

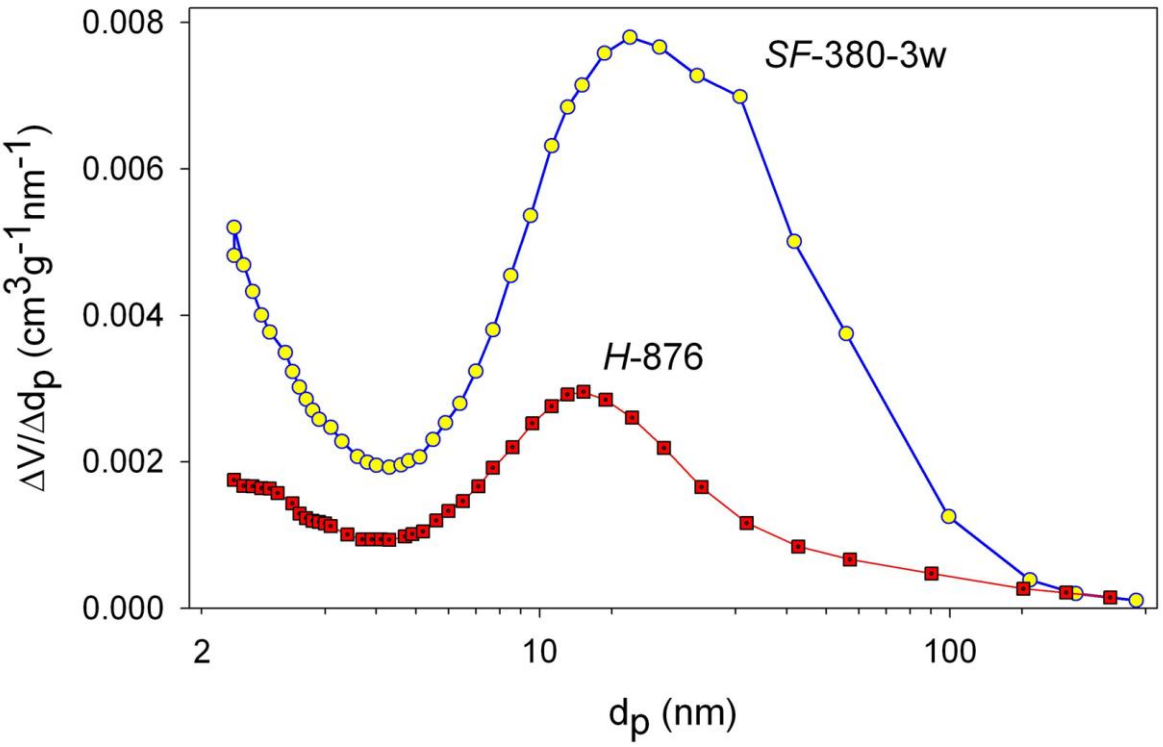

EPDIC15_Proc._Peplinski_Figure S7_(2017-05-16, 0.5 MB).tif